OPEN

Correspondence and
requests for materials
should be addressed to
Y.S.C. (yschen@aphy.
iphy.ac.cn) or J.R.S.
(jrsun@iphy.ac.cn)

Evolution of conduction channel and its effect on resistance switching for Au-WO$_{3-x}$–Au devices

D. S. Hong, Y. S. Chen, Ying Li, H. W. Yang, L. L. Wei, B. G. Shen & J. R. Sun

Beijing National Laboratory for Condensed Matter Physics and Institute of Physics, Chinese Academic of Sciences, Beijing 100190, China.

We performed a systematic investigation on the dynamic behavior of conduction filaments (CFs) in WO$_{3-x}$-based devices. It was found that the electric forming produced an electric structure consisted of a conductive channel (virtual cathode) started from cathode and an insulating band surrounding anode. Both the virtual cathode and the insulating region varied with repeated resistance switching. Set/reset operation affected device resistance mainly by modifying the CF, which formed in the setting process together with an insulating halo that separated it from the virtual cathode. The device resistance exhibited a sudden change exactly corresponding to the emergence/vanishing of the CF and a smooth variation corresponding to the outward/inward expansion/contraction of the insulating halo. Anode ablation occurred after repeated cycling, and it is the key factor affecting the endurance of device.

Electric field-induced resistance switching (RS) between a high and a low resistance state (HRS and LRS) in dielectric material, which is a phenomenon discovered 40 years ago[1], has received renewed interest in recent years due to its prospective application in non-volatile memory as well as other information technologies[2–5]. This effect has been widely observed in metal-insulator-metal (MIM) stacks with the insulator of either oxide or electrolyte. Although the material are different, the mechanisms for the RS seem to be common, i.e., the formation or rupture of nanometer-sized conduction filaments (CFs)[6–8]. Solid evidence for the presence of CFs has been obtained by various techniques[9–17]. For example, optical microscope observed a field-induced directional growth of Ag chains in Ag$_2$S$_3$ films[9]. Transmission electron microscope (TEM) captured the processes of the formation and rupture of Ag-based CFs in oxide matrix[13–16]. Although oxygen vacancy (V$_O$) is invisible for most techniques, signatures of V$_O$-based CFs were still identified: While repeating the RS operation, a development of gas bubbles underneath anode was observed in the Au-SrTiO$_3$ system[10]. A high resolution image of V$_O$-CF, i.e., nanometer-sized Ti$_n$O$_{2n-1}$ filament, was also obtained by the TEM technique in a Pt/TiO$_2$/Pt cell[17].

CFs assign the RS effect two important features, i.e., excellent scale-down capability, the RS effect keeps strong in nanometer-sized devices, and high speed, the RS accomplishes within nanoseconds. Both characteristics are promising for information storage. However, the CFs have drawbacks of themselves. Due to their unpredictable locations and irregular structures, the switching parameters of the RS device, including set/reset voltage and HRS/LRS resistance, often dispersed in a wide range. The endurance of the device was also miserable, and sometimes an electric breakdown happened within a few switching cycles.

After intensive studies, it becomes more and more clear that the regulation of the CF is the key issue for the improvement of device performance. Unfortunately, our knowledge about the CFs, which is obviously a prerequisite for an effective CF controlling, is still very limited, particularly the knowledge about the dynamic characters of the CFs, and some important issues remain unaddressed, such as what has happened to the CFs while repeating the RS operations, what is the crucial factor affecting the switching parameters, and what resulted in the RS failure. Obviously, the answer to these questions relies on a thorough understanding of the dynamic RS process.

TEM technique equipped with an electrical measurement unit provides a feasible approach monitoring the evolution of the CF in the RS process. However, the performance of the TEM sample is usually inferior to its bulk counterpart, which makes a systematic investigation difficult. Conductive atomic force microscope (C-AFM) is also a high resolution technique for detecting CFs[12]. However, the data quality strongly depends on tip quality which is usually deteriorated after repeated scanning. By contrast, optical microscope is a promising technique for dynamic study since this technique and the corresponding sample allow a unconditional repetition of the RS
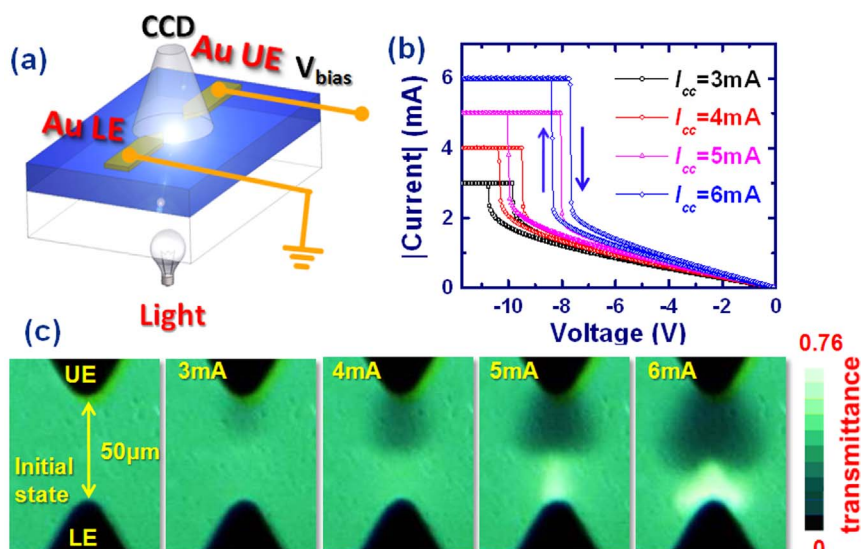
Figure 1 | (a) Experiment setup for optical observation. (b) I-V relations for four electric forming processes with the current compliances of $I_{CC} = 3$ mA, 4 mA, 5 mA and 6 mA, respectively. (c) Transparent photographs corresponding to the above forming processes. All the optical microscopic images were recorded after the application of I_{CC}. Black shadow appears when $I_{CC} = 3$ mA, but the bright band is ambiguous until $I_{CC} = 5$ mA. Electrode separation is 50 μm.

operation. If an appropriate material possessing electrochromic character can be found, the dynamic process of the RS there could be readily captured by photo microscope. Although the CFs in a laterally structured optical sample could be different from those in a MIM-stacked sample, the mechanisms for the RS should be the same. CMOS-compatible material $WO_{3-\delta}$ ($\delta \ll 0.1$), which is a potential candidate for intelligent nano-devices with unique electro-resistive/neuromorphic properties[18–20], is a suitable material. Due to the electrochromic characteristics (the transmittance is reduced when W^{5+} ions appear), CFs in $WO_{3-\delta}$ could be discriminated from background by color contrast, and therefore could be recorded by photo microscope. Combining photo microscopy with synchronous electric measurements, here we performed a systematic investigation on the Au-WO_{3-x}-Au lateral device ($x > \delta$), focusing on the correlation between the microscopic structure of the CFs and the macroscopic properties of the RS devices. We found that electric forming yielded an electric structure composed of a conduction channel (virtual cathode) stemmed from cathode and an insulating layer around anode. The set/reset operation affected strongly the insulating layer and fairly the virtual cathode. The correspondence between the CFs and the resistance state, including intermediate states during the RS, was determined. Evolution of the CF in structure/location against repeated RS operations was tracked, and the key factors affecting the endurance of the Au-WO_{3-x}-Au were identified.

## Results and discussions

A series of Au-WO_{3-x}-Au devices, with the electrode-electrode (Au-Au) separations of 20 μm or 50 μm, were prepared for the present research. Figure 1(a) is a schematic view of the experiment setup. For convenience, we defined the two electrodes as upper electrode (UE) and lower electrode (LE), respectively. Electric bias was applied to the UE and the LE was grounded. All measurements were performed in dry air at ambient temperature. To perform electric forming, a negative field was applied to the UE, and the resulted changes in current and transparency were simultaneously recorded. With the increase of bias voltage, the current undergoes first a linear and then an abrupt growth (Fig. 1(b)). Exactly corresponding to the accelerated current growth, a shadow area appears in front of the UE and expends rapidly to the LE. Simultaneously, a narrow and bright bar against the shadowed area emerges in front of the LE (data for $I_{cc} = 5$ mA in

Fig. 1(c)) and laterally spreads under the stress of the dark channel (data for $I_{cc} = 6$ mA in Fig. 1(c)), protecting the LE against being shadowed. By the end of the forming process, a structure consisted of a broad dark channel and a narrow bright band around the LE is formed. The transmittance images in Figs. 1(c) demonstrate the detailed process of electric forming.

To specify the electric structure caused by forming process, Raman spectroscopy of the sample was measured. Figure 2(a) is the typical transmittance image of electrically formed Au-WO_{3-x}–Au cell. Fig. 2(b) presents the Raman spectra collected at the locations marked by red circles in Fig. 2(a). Data of a nearly stoichiometric $WO_{3-\delta}$ ($\delta \ll 0.1$, prepared under a high oxygen pressure of 30 Pa) were also given for comparison. From first glance, the spectra of the bright and dark regions are similar to those of $WO_{3-\delta}$ and WO_{3-x}, respectively. A quantitative analysis of the Raman spectra can be obtained by multi-component spectral fitting (see Support Information, Fig. S1). It is found that, from dark to bright regions, the ~ 811 cm^{-1} peak (W^{6+}) grows by fivefold whereas the ~ 427 cm^{-1} peak (W^{5+}) reduces by 80% (Fig. 2(c))[21], i.e., the electron density in dark region is higher than that in bright region. It is possible that oxygen anions are pushed by electric field from UE to LE (see Support Information for detailed analyses, Fig. S2), forming oxygen-deficient region near the UE and oxygen-excessive region around the LE. Based on the relation between oxygen content and transmittance established by Yamamoto et al.[22], the distribution of oxygen vacancies in WO_{3-x} can be obtained. Expressing the bright region as $WO_{3-\delta}$ (This region exhibits similar transmittance and Raman spectrum with those of $WO_{3-\delta}$), as shown in Fig. 2(d), the darkest region is then $WO_{2.7-\delta}$, near the metal-semiconductor border[23]. From bright to dark regions, the content of oxygen vacancies increases from 0 to 0.3, corresponding to the increase (decrease) of the content of W^{5+} (W^{6+}) ions from $\sim 0\%$ to $\sim 80\%$ ($\sim 100\%$ to $\sim 20\%$). This result is compatible with that of Raman spectra. It is therefore clear that the electric forming generates an electric structure composed of a broad conductive channel stemming from cathode (virtual cathode) and a narrow insulating shell around anode. It is similar to the case for the MIM-stacked devices with an active anode, for which electric forming created an oxide shell around anode[24,25].

Indeed, this kind of electric structure supports the RS. As exemplified in Fig. 3(a), the I-V characteristics of the Au-WO_{3-x}-Au cell

2
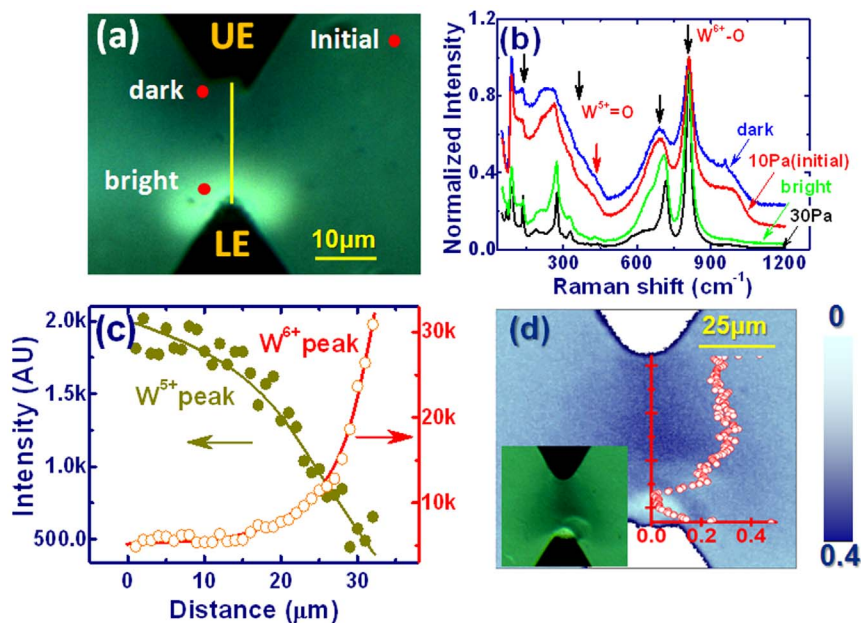
Figure 2 | (a) Transmittance image of electrically formed Au-WO_{3-x}–Au cell. Red circles and yellow midline indicate the locations for Raman measurements. (b) Normalized Raman spectra collected from the dark and bright regions of electrically formed WO_{3-x} (10 Pa). Data for pristine $WO_{3-\delta}$ (30 Pa) and WO_{3-x} (10 Pa) films are also shown for comparison. (c) Intensity variation of $\sim$427 cm^{-1} and $\sim$811 cm^{-1} peaks along the midline between two electrodes. (d) Mapping of oxygen vacancies for electrically treaded WO_{3-x} cell, derived from the transmittance image shown in the inset. The inset curve shows the distribution of oxygen vacancies along midline.
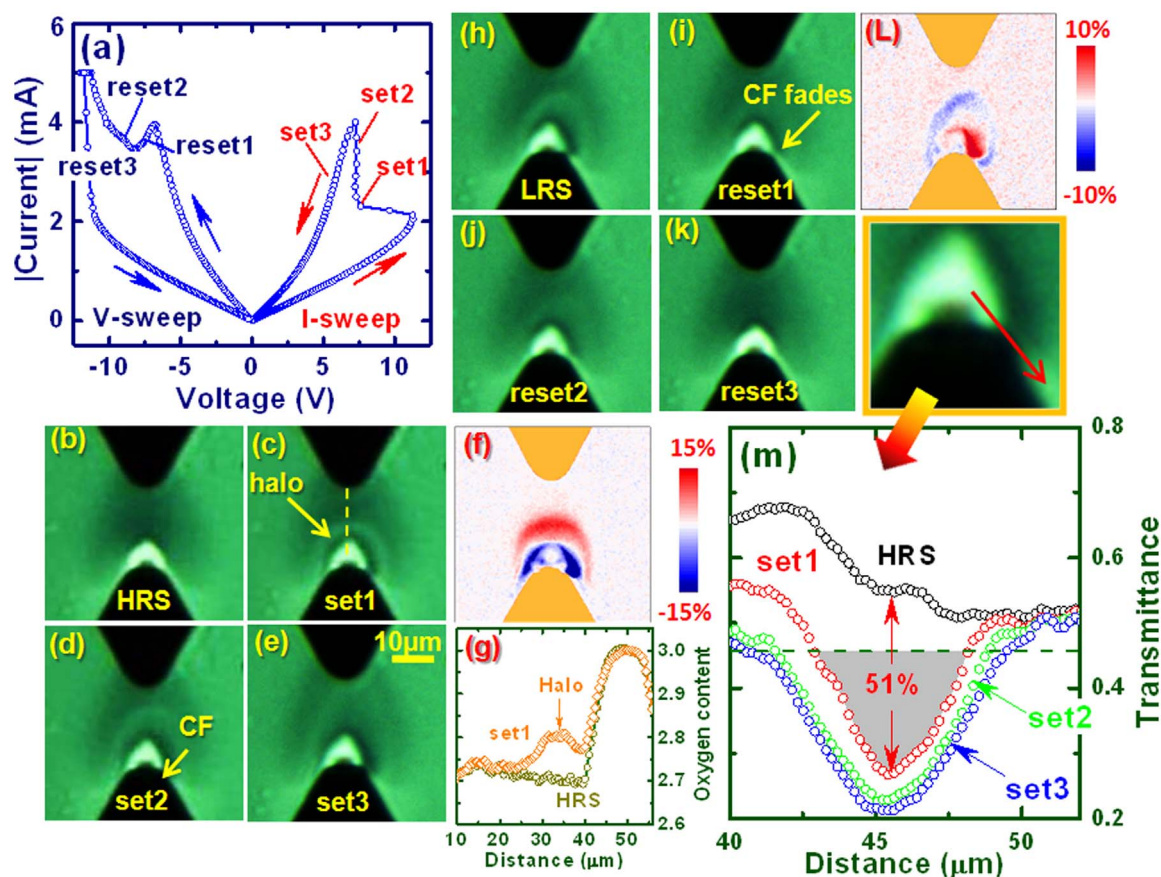
Figure 3 | (a) I-V characteristics of a device set by current sweeping (positive biases) and reset by voltage sweeping (negative biases). Labels mark the different stages of set/reset process. (b)–(e) and (h)–(k) Two series of transmittance images corresponding to the intermediate states in the set and reset processes, respectively. (f) and (L) Relative variations of color contrast from the HRS to set1 (f) and from the LRS to reset1 (L); expansion/contraction of the fine CF and the faint halo can be clearly seen. (g) Oxygen content measured along the dashed line in (c); the dark-bright border exhibits lowest oxygen content, $\sim$2.7 in the as-formed state, and the faint halo (marked by an arrow in (c)) owns an oxygen content of $\sim$2.8. (m) Line-profile of the transmittance of the CF, collected along the arrow marked in the upper-right image. Shaded area marks the CF, and the number denotes the maximal transmittance drop.

show the typical feature of bipolar RS. The sharp voltage drop started at ~11.3 V signifies the HRS-LRS transition, and the reset process is indicated by a sudden current drop at −7.1 V. The set process can be clearly classified into two distinctive processes marked by respectively a sudden voltage drop (set1) and a followed abrupt current jump (set2). There is no obvious signature for the finishing of the set process, whereas the ending of the reset one is marked by the current upturn (reset2) following the current drop (reset1). Exactly corresponding to the sharp voltage drop of set1, as revealed by in situ optical observation, a CF was formed across the insulating layer (Fig. 3(c)). Since the insulating layer is thick in front of the LE, the CF grew on one side rather than the apex of the LE, though the electric field near apex may be the strongest. A line-profile analysis indicates that the CF is ~5 μm in width, with a transmittance of ~51% lower than neighboring region (Fig. 3(m)). Accompanying the formation of the CF, an additional annular halo outside the insulating layer emerged, separating the CF from virtual cathode. After repeated experiments for various samples, we found that, fascinatingly, the CF always appeared with a halo cap, regardless of device structure. According to the profile analysis in Fig. 3(g), the dark-bright border is most conductive. The CF joined this border while breaking through the insulating layer, forming a arc-like electrode that shunts the LE. Meanwhile, the oxygen vacancies near this border were pushed by the arc-like electrode to the UE, forming a bright halo. The annular form of the halo indicated that the field distribution between two electrodes was rather symmetric. Fig. 3(f) shows the change in oxygen distribution from HRS to set1. Blue (red) color represents the region where oxygen content is decreased (increased) after set1. It displays a significant reduction of oxygen content in the region near LE (blue-colored regions), especially on the right side of the CF where the CF formed, and an accumulation of oxygen ions in the region in close proximity of the blue arc. A quantitative analysis shows that the number of the oxygen ions expelled from the blue region is ~6.8×10^{11} while the accepted oxygen ions by the red region is ~7.3×10^{11}, i.e., a portion of oxygen ions in blue area were driven to red region by the set operation, and the oxygen content of the film remained unchanged. According to the line profile data in Fig. 3(g), the oxygen content is ~2.7 at bright-dark border in the HRS state and ~2.8 in the faint halo in the state after set1; the latter is a value in between those of the bright and dark regions.

With the continuous growth of the set current, the width/transparency of the CF changed only slightly. The transmittance reduction is ~7% from set1 to set2 (Fig. 3(m)), in contrast to the sharp drop from HRS to set1. Meanwhile, the CF width (measured along the dashed line in Fig. 3(m)) grew by ~20%. Obviously, the darkening and widening of CF are responsible for the continuous conduction increase from set1 to set2. A remarkable observation is the continuous expansion of the annular halo from Figs. 3(c) to 3(e). It indicates a back-flow of oxygen ions, driven by setting field. Removing set current gradually, the I-V curve goes back along an alternative trajectory, which may be ascribed to slight changes in electric structure (Figs. 3(d) to 3(e)). A strong influence of electric structure on transport property is also observed in the reset process. As expected, the reset process is exactly an opposite process of the set one, i.e., the CF dissolved and the halo contracted (Figs. 3(h)–3(k)).

The fine electric structure of the device is particularly interesting. We have repeated our experiments for differently structured samples, and observed similar phenomena, i.e., rather than directly penetrating into virtual cathode, the CF prefers to appear with an insulating cap (bright halo). After a careful analysis of the correspondence in Fig. 3(a) and Figs. 3(b)–3(e), we found that the faint halo played a distinct role in the controlling of the RS process: It separates the CF from virtual cathode, thus prevents an electric breakdown due to the sudden appearance of the CF, which makes it available for the regulation of current growth.

As a supplement, we would like to point out that the RS behavior here is different from that observed in stacked Pt/WO₃/Pt devices, where the insulating layer around the anode was broken when oxygen anions were pushed to and then absorbed by Pt[26]. In that case, electrode acted as oxygen reservoir, exchanging oxygen ions with the active layer. In contrast, the electrode in Au-WO$_{3-x}$-Au is unnecessarily oxygen-soluble since the CF grows from the anode instead of virtual cathode. In fact, the RS in our samples is similar to that in devices with a reactive electrode such as Al-Pr$_{0.7}$Ca$_{0.3}$MnO₃[24]. As reported, to drive the device to the LRS, a reverse field has to be applied to dissolve the AlO$_x$ insulating layer that was formed during electric forming.

In addition to the close relation between electric structure and resistance state, above experiments reveals a strong influence of the set/reset operation on electric structure. It is then an interesting issue what will happen to electric structure while repeating RS cycles again and again. In Fig. 4(a) we show the HRS/LRS resistance as a function of cycle numbers, derived from the I-V curves at a bias of 0.5 V. Look at the sample with the 40-nm-thick Au electrodes. The resistance of the HRS undergoes a decrease at a rate of ~0.008% per cycle up to 1300 cycles. Different from the HRS, resistance of the LRS experiences first a slow decrease and then a smooth increase, above ~600 cycles. Accompanying this resistance upturn, considerable data fluctuation appears and develops, severely deteriorating the performance of the device. As an example, the I-V curves from 200 to 400 cycles are presented in Fig. 4(b). Fig. 4(c) is a comparison of the resistance distributions from 200 to 400 cycles and from 800 to 1000 cycles. Obviously, device performance is much better in the former 200 cycles.

From in situ optical observation, we can get direct information about the electric structure. As shown by Figs. 4(d) to 4(g), the virtual cathode exhibits a lateral expansion and a detectable coloring after the first several hundreds of cycles (Figs. 4(d) and 4(e)), then the apex of the LE becomes transparent with further cycling (Figs. 4(e) to 4(g)). Meanwhile, the location of the CF becomes uncertain, switching between the left and right sides of the LE. Sometimes two CFs, with one on each side of Au, appear (Fig. 4(g)). To trace the evolution of the electric structure, in Figs. 4(h) and 4(i) we present the transmittance changes with electric switching, obtained by subtracting the image of 10 cycles from those recorded after 50 and 400 cycles, respectively. It shows that, while repeating the RS, lung-shaped blue areas (marked by red arrow in Fig. 4(i)) appear and develop on two sides of the virtual cathode. The maximal transmittance change is ~12% after 400 cycles, occurring on right side of the anode (opposite to the CF, marked by yellow arrow). As a consequence, the effective width of the virtual cathode was nearly doubled. In contrast, the width and transparency of the CF remains essentially unchanged as indicated by the line-profile analysis in Fig. 4(j). These results indicate that the resistance decrease in the first several hundreds of cycles in Fig. 4(a) is actually a consequence of structure reconstruction of the virtual cathode. While the performance worsening could be ascribed to the random location of the CF and the appearance of multi-CFs. Compared with HRS, the LRS is more sensitive to the details of the CF. Therefore, its resistance fluctuates more strongly against electric cycling.

To identify the source for data fluctuation, the surface morphology of the Au electrode was analyzed. As shown by the AFM image in Fig. 5(a), the Au layer is smooth just after the forming process, and only its front edge is slightly blurred. After hundreds of cycles, however, a visible gap appears and develops in the apex of the LE and, in the meantime, the residual Au film surrounding this gap is significantly coarsened. This could be a consequence of self Joule heating[27,28] or gas release due to the oxidation of oxygen anions underneath anode[10]. The latter may be the main reason for electrode ablation since it occurred at the apex of the electrode rather than the left side where the CF formed (marked by an arrow in Fig. 5(c)).
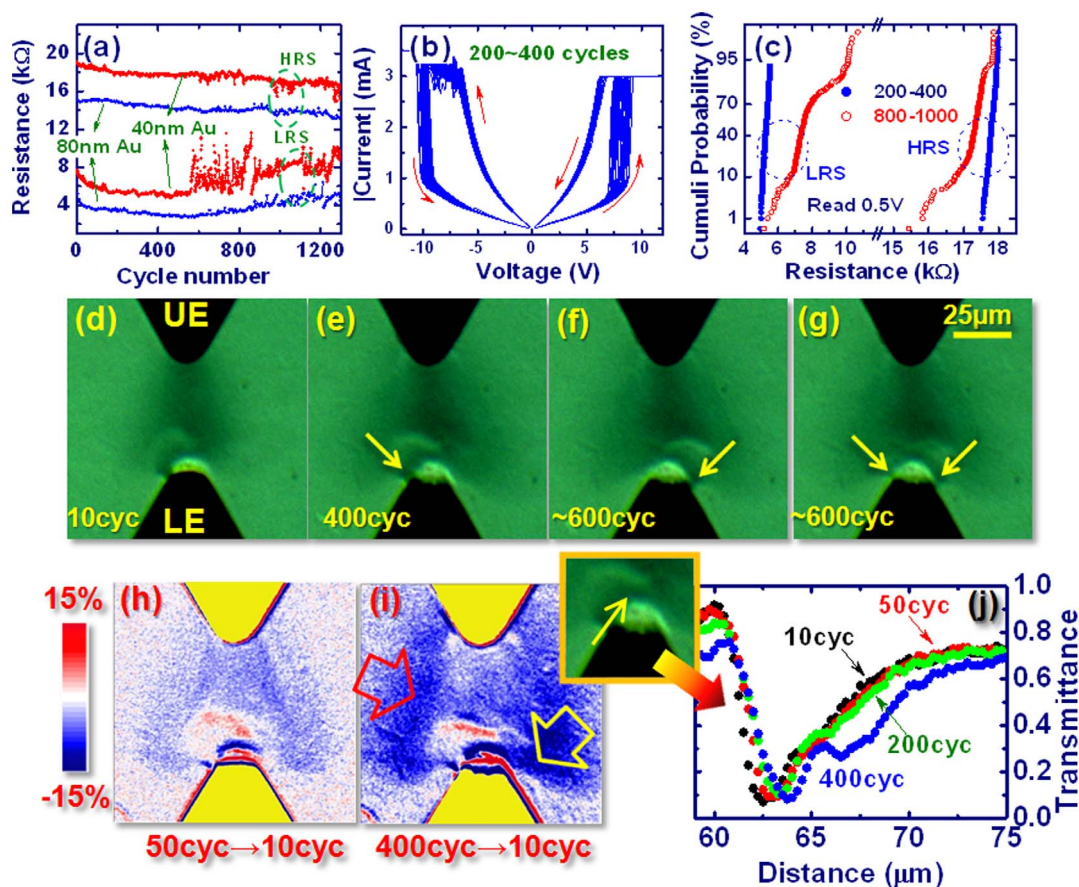
Figure 4 | (a) Endurance performance of the Au-WO$_{3-x}$-Au cell. Red and blue curves correspond to the devices with the Au electrodes of 40 nm and 80 nm, respectively. (b) I-V characteristics from 200 to 400 cycles. (c) Cumulative distributions of the device resistance, counted from 200 to 400 and 800 to 1000 cycles, respectively. (d)–(g) Transmittance images of the device after 10, 400, ~600 electric cycles (LRS). Random CF location appears and, sometimes, more than one CF are formed above 600 cycles. (h) and (i) Relative transmittance change after different RS cycles. Arrows in (i) mark the two strips appearing after repeated cycles. (j) Line profiles of the transmittance of the CF, measured along the direction marked by an arrow in the upper-left image.

Obviously, electrode ablation will make the field distribution near the LE irregular, modifying the structure of the CF. In return, the feedback of the multi-CF effect will further deteriorate field distribution, enhancing the uncertainty of the RS behavior. As a result, the performance of the device becomes worse and worse until a hard electric breakdown occurs. According to this analysis, if an approach depressing electrode ablation can be found, the device performance should be improved. By using thicker Au electrodes, we indeed obtained improved device endurance. For example, increasing Au thickness from 40 nm to 80 nm, the number of stable RS cycles grows from ~600 to ~1200 cycles (blue symbols in Fig. 4(a)). Obviously, a thicker Au film has a better mechanical strength, withstanding the impact of O$_2$ gas formed underneath the anode. Meanwhile, the thickness increase of Au will enhance the conductance of the electrode, thus reduce the Joule heat. It is expected that the current will flow through electrode as far as possible since the resistance of Au is lower than that of WO$_{3-x}$. However, the electrode resistance will continuously grow approaching the apex due to the reduction of the width of Au, and the current will finally flow perpendicularly into WO$_3$. A thicker Au could postpone the occurrence of the latter process, i.e., the current may advance further along Au before flowing into the WO$_3$. As a result, the damaged area will be shrunk and its effect on field distribution will be depressed. This explains why only an increase of thickness by a factor of two considerably improved device performance. These results indicated that electrode was a key factor affecting the performance of the Au-WO$_{3-x}$-Au devices.

In summary, the dynamic process of the RS in Au-WO$_{3-x}$-Au device was systematically studied by means of in situ optical observation and electric measurements. We found that electric forming causes a redistribution of the oxygen vacancies in WO$_{3-x}$, yielding an electric structure consisted of a conductive channel stemmed from cathode and an insulating layer around anode. Set/reset operation affects both the insulating layer and the virtual cathode, yielding/dissolving a CF in insulating layer in the meantime driving an outward/inward expansion/contraction of an insulating halo in virtual cathode. Exactly corresponding to the emergence/vanishing of the CF, device undergoes a sudden resistance change. Repeated electric switching causes a significantly lateral expansion of virtual cathode and a redistribution of the W^{6+}/W^{5+} ions between two electrodes but
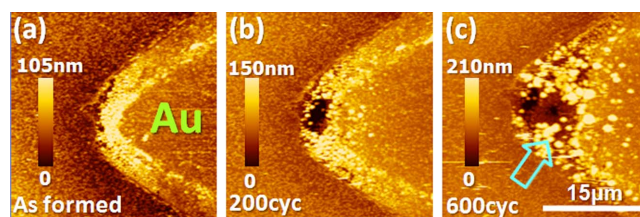
Figure 5 | Surface morphology of the LE immediately after the (a) forming process, (b) 200 switching cycles, and (c) 600 switching cycles. The ablated region in the LE expands with switching cycles. Arrow in (c) marks the location of CF.

5

affects slightly CF until the electrode ablation. The latter is a key factor affecting the endurance performance of the Au-WO$_{3-x}$-Au devices.

Methods

Device fabrication and measurement. Planar Au/WO$_{3-x}$/Au devices were composed of a WO$_{3-x}$ blanket layer covering the entire glass wafer and arrow-shaped Au electrodes above the film. The WO$_{3-x}$ layer was prepared by pulsed laser deposition from a WO$_{3-\delta}$ target. The film thickness was ~600 nm, controlled by deposition time (deposition rate = 10 nm/min). During the deposition, the substrate temperature was held at 400°C and the oxygen pressure at 10 Pa. 40-nm- or 400-nm-thick Au layers were deposited by DC sputtering on the WO$_{3-x}$ film covered by arrow-shaped photo-resist patterns, and electrode arrays were fabricated by the conventional lithography and lift off technique. Two series of Au-WO$_{3-x}$-Au devices, with two electrode-electrode separations of 20 μm and 50 μm, respectively, were prepared for the present experiments. The DC characteristics of device were measured by a Keithley 2611 source meter at ambient temperature in dry air.

Optical observation and AFM & Raman analyses. In the same time of electric characterization, the sample was illuminated by white light on the back and the transparency was recorded by a CMOS camera through an intermediate photomicroscope. The surface morphology of the WO$_{3-x}$ film was analyzed by a atomic force microscope (AFM, Seiko Instruments, SPA400) with a Si tip. The valence state of tungsten ion in the WO$_{3-x}$ film was characterized by a confocal micro-Raman spectrometer (Horiba/Jobin Yvon HR800), using the 532 nm excitation laser line (beam spot size = 1 μm). Transmittance of the WO$_{3-x}$ film was determined by comparing the light intensities through the glass with WO$_{3-x}$ and glass alone, respectively. Distribution of oxygen vacancies was deduced from the transmittance image collected under a monochromatic light of 633 nm, adopting the transmittance-oxygen content relation established by Yamamoto et al. in Ref. 22.

1. Dearnaley, G., Stoneham, A. M. & Morgan, D. V. Electrical phenomena in amorphous oxide films. *Rep. Progr. Phys.* **33**, 1129–1140 (1970).
2. Liu, S. Q., Wu, N. J. & Ignatiev, A. Electric-pulse-induced reversible resistance change effect in magnetoresistive films. *Appl. Phys. Lett.* **76**, 2749–2751 (2000).
3. Baek, I. G. et al. Highly scalable nonvolatile resistive memory using simple binary oxide driven by asymmetric unipolar voltage pulses. 50th IEEE International Electron Devices Meeting, San Francisco CA. IEEE International electron devices meeting 2004, Techical Digest, 587–590: IEEE (2004, Dec. 13–15).
4. Waser, R. & Aono, M. Nanoionics-based resistive switching memories. *Nat. Mater.* **6**, 833–840 (2007).
5. Strukov, D. B., Snider, G. S., Stewart, D. R. & Williams, R. S. The missing memristor found. *Nature* **435**, 80–83 (2008).
6. Lee, S. B. et al. Scaling behaviors of reset voltages and currents in unipolar resistance switching. *Appl. Phys. Lett.* **93**, 212105 (2008).
7. Yang, Y. C., Pan, F., Liu, Q., Liu, M. & Zeng, F. Fully Room-Temperature-Fabricated Nonvolatile Resistive Memory for Ultrafast and High-Density Memory Application. *Nano Lett.* **9**, 1636–1643 (2009).
8. Waser, R., Dittmann, R., Staikov, G. & Szot, K. Redox-Based Resistive Switching Memories -Nanoionic Mechanisms, Prospects, and Challenges. *Adv. Mater.* **21**, 2632–2663 (2009).
9. Hirose, Y. & Hirose, H. Polarity-dependent memory switching and behavior of Ag dendrite in Ag-photodoped amorphous As$_2$S$_3$ films. *J. Appl. Phys.* **47**, 2767–2772 (1976).
10. Szot, K., Speier, W., Bihlmayer, G. & Waser, R. Switching the electrical resistance of individual dislocations in single-crystalline SrTiO$_3$. *Nat. Mater.* **5**, 312–320 (2006).
11. Janousch, M. et al. Role of Oxygen Vacancies in Cr-Doped SrTiO$_3$ for Resistance-Change Memory. *Adv. Mater.* **19**, 2232–2235 (2007).
12. Szot, K., Reichenberg, B. & Peter, F. Electrical characterization of perovskite nanostructures by SPM, In *Scanning Probe Microscopy*, Kalinin, S. & Gruverman, A. (ed.), 746–775 (Springer, Heidelberg/Berlin, 2007).
13. Guo, X., Schindler, C., Menzel, S. & Waser, R. Understanding the switching-off mechanism in Ag$^+$ migration based resistively switching model systems. *Appl. Phys. Lett.* **91**,133513 (2007).
14. Hsiung, C. P. et al. Formation and Instability of Silver Nanofilament in Ag-Based Programmable Metallization Cells. *ACS Nano* **4**, 5414–5420 (2010).
15. Liu, Q. et al. Real-Time Observation on Dynamic Growth/Dissolution of Conductive Filaments in Oxide-Electrolyte-Based ReRAM. *Adv. Mater.* **24**, 1844–1849 (2012).
16. Yang, Y. C. et al. Observation of conducting filament growth in nanoscale resistive memories. *Nat. Commun.* **3**, 732–739 (2012).
17. Kwon, D. H. et al. Atomic structure of conducting nanofilaments in TiO$_2$ resistive switching memory. *Nat. Nanotechnol.* **5**, 148–153 (2010).
18. Bechinger, C., Oefinger, G., Herminghaus, S. & Leiderer, P. On the fundmental role of oxygen for the photochromic effect of WO$_3$. *J. Appl. Phys.* **74**, 4527–4533 (1993).
19. Szilagyi, I. M. et al. Stability and controlled composition of hexagonal WO$_3$. *Chem. Mater.* **20**, 4116–4125 (2008).
20. Yang, R. et al. On-demand nanodevice with electrical and neuromorphic multifunction realized by local ion migration. *ACS Nano.* **6**, 9515–9521 (2012).
21. Lee, S. H. et al. Electrochromic mechanism in α-WO$_{3-y}$ thin films. *Appl. Phys. Lett.* **74**, 242–244 (1999).
22. Yamamoto, S., Takano, K., Inouye, A. & Yoshikawa, M. Effects of composition and structure on gasochromic coloration of tungsten oxide films investigated with XRD and RBS. *Nucl. Instr. and Meth.* in *Phys. Res. B* **262**, 29–32 (2007).
23. Ingham, B., Hendy, S. C., Chong, S. V. & Tallon, J. L. Density-functional studies of tungsten trioxide, tungsten bronzes, and related systems. *Phys. Rev. B* **72**, 075109 (2005).
24. Seong, D. et al. Resistive-switching characteristics of Al/Pr$_{0.7}$Ca$_{0.3}$MnO$_3$ for nonvolatile memory applications. *IEEE Electron Device Lett.* **30**, 919–921 (2009).
25. Jeong, H. Y., Lee, J. Y. & Choi, S. Y. Interface-Engineered Amorphous TiO$_2$-Based Resistive Memory Devices. *Adv. Funct. Mater.* **20**, 3912–3917 (2010).
26. Yang, R., Terabe, K., Tsuruoka, T., Hasegawa, T. & Aono, M. Oxygen migration process in the interfaces during bipolar resistance switching behavior of WO$_{3-x}$-based nanoionics devices. *Appl. Phys. Lett.* **100**, 231603(2012).
27. Tran, X. A. et al. High performance unipolar AlO$_y$/HfO$_x$/Ni based RRAM compatible with Si diodes for 3D application. *Symp. VLSI Technology* **44** (2011).
28. Cao, M. G. et al. Nonlinear dependence of set time on pulse voltage caused by thermal accelerated breakdown in the Ti/HfO2/Pt resistive switching devices. *Appl. Phys. Lett.* **101**, 203502 (2012).

Acknowledgments

Author contributions

J.R.S. and Y.S.C. conceived and designed the experiments, analyzed and interpreted the data. D.S.H. carried out the experimental measurements. Y.L. And L.L.W. made the AFM characterizations of the sample. H.W.Y. performed some calculations. Y.S.C. drafted the manuscript, and J.R.S. wrote and edited the manuscript. B.G.S. oversaw the project. All authors commented on the manuscript.

Additional information